ELSEVIER

Volume 187, March 2012

CONTENTS

JOURNAL OF SOLID STATE CHEMISTRY

www.elsevier.com/locate/jssc

Abstracted/indexed in BioEngineering Abstracts, Chemical Abstracts, Coal Abstracts, Current Contents/Physics, Chemical, & Earth Sciences, Engineering Index, Research Alert, SCISEARCH, Science Abstracts, and Science Citation Index. Also covered in the abstract and citation database SciVerse SCOPUS®. Full text available on SciVerse ScienceDirect®.

Regular Articles

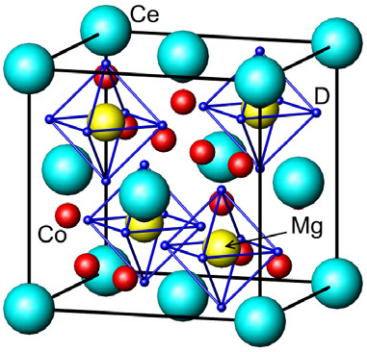

Crystal structure of the β-$CeMgCo_4D_{4.2}$ deuteride. Octahedra of *D*-sites around Mg atoms are shown.

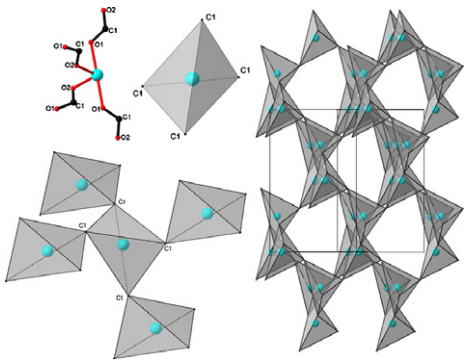

$[Cu(O_2C–CH_2–CO_2H)_2 \cdot 2H_2O]$: the first 3D hybrid organic–inorganic compound built up carboxyl groups. The network presents a diamond-like structure achieved via carboxyl.

Regular Articles—Continued

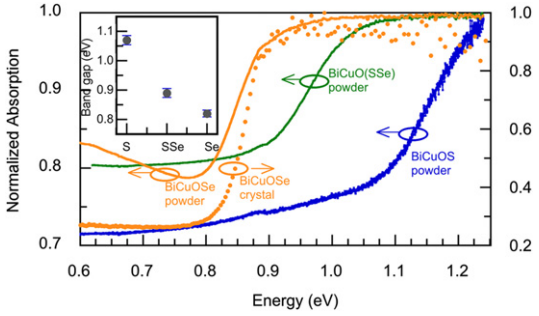

IR absorption of BiCuO*Ch* powders from diffuse reflection (left scale) and polished BiCuOSe single crystal from transmission (right scale). Spectra are normalized to the maximum absorption. Inset: band gap as a function of composition.

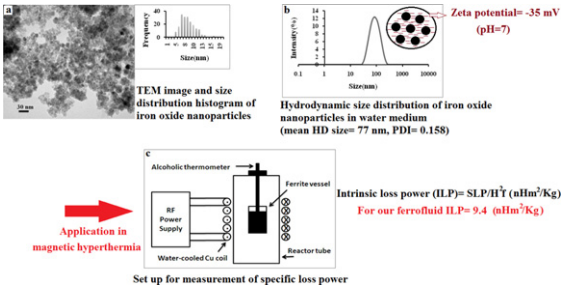

Monodispersed aqueous ferrofluids of iron oxide nanoparticles were synthesized by hydrothermal-reduction method with citric acid as reductant which is an efficient way to synthesize aqueous ferrofluids applicable in magnetic hyperthermia.

Continued

Neutron diffraction study of the monoclinic to tetragonal structural transition in $LaNbO_4$ and its relation to proton mobility

M. Huse, A.W.B. Skilbred, M. Karlsson, S.G. Eriksson, T. Norby, R. Haugsrud and C.S. Knee

page 27

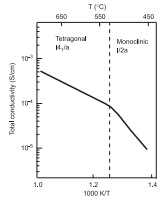

The structural phase transition from monoclinic fergusonite to tetragonal scheelite crystal structure clearly influences the proton conductivity of acceptor-doped $LaNbO_4$ (see Figure). The present article attempts to explain why.

Crystal structure and characterization of the novel $NH^+\cdots N$ hydrogen bonded polar crystal $[NH_2(CH_2)_4NH][BF_4]$

M. Wojtaś, A. Gągor, O. Czupiński, W. Medycki and R. Jakubas

page 35

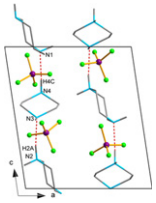

It must be emphasized that the titled compound represents the first organic–inorganic simple salt containing the single-protonated piperazinium cation which was studied by means of the wide variety of experimental techniques. A survey of Cambridge Structural Database (CSD version 5.32 (November 2010) & updates (May 2011)) for structure containing the piperazinium cations yields 248 compounds with the doubly protonated piperazinium(2+) cations and only eight compounds with the singly protonated piperazinium(+) cations. Among these structures only one is the hybrid organic–inorganic material. This is piperazinium nitrate characterized structurally.The crystal packing of $[NH_2(CH_2)_4NH][BF_4]$, phase IV. The dashed lines stand for the hydrogen bonds. The hydrogen bonds to BF4 groups are not included for the picture quality.

Synthesis, phase composition modification, and optical properties of Ce^{3+}/Tb^{3+} activated $KGdF_4$ and GdF_3 submicrocrystals

Chunyan Cao, Hyun Kyoung Yang, Byung Kee Moon, Byung Chun Choi, Jung Hyun Jeong and Kwang Ho Kim

page 45

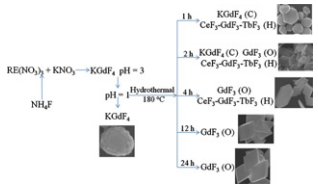

Schematic illustration for the phase composition modification from the Ce^{3+}/Tb^{3+} doped $KGdF_4$ to the Ce^{3+}/Tb^{3+} doped GdF_3 with multiform morphologies and different sizes. (C presents cubic phase, H presents hexagonal phase, and O presents orthorhombic phase.)

Introduction of oxygen vacancies and fluorine into TiO_2 nanoparticles by co-milling with PTFE

Mamoru Senna, Vladimir Šepelák, Jianmin Shi, Benjamin Bauer, Armin Feldhoff, Vincent Laporte and Klaus-Dieter Becker

page 51

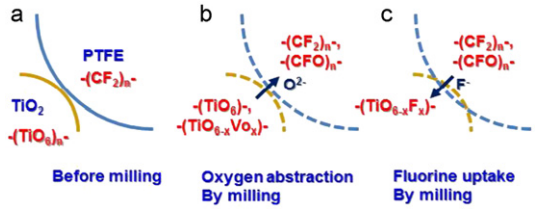

Scheme of the reaction processes: (a) pristine mixture, (b) oxygen abstraction from TiO_2 and (c) fluorine migration from PTFE to TiO_2.

Facilitating ZnO nanostructure growths by making seeds for self-catalytic reactions

Liang Yin and Choongho Yu

page 58

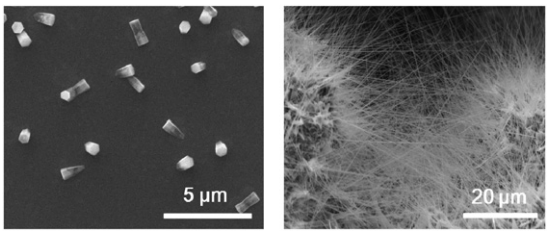

(Left panel) ZnO seeds from $ZnCl_2$ after thermal annealing at 500 °C for 5 min, (right panel) dense ZnO nanowires grown from Zn foils with $ZnCl_2$ coating after thermal annealing at 700 °C for 60 min.

Atomic Pt and molecular H_2O adsorptions on $SrTiO_3$ with and without Nb-doping: Electron trapping center and mediating roles of Pt in charge transfer from semiconductor to water

Wei Wei, Ying Dai, Meng Guo, Yandong Ma and Baibiao Huang

page 64

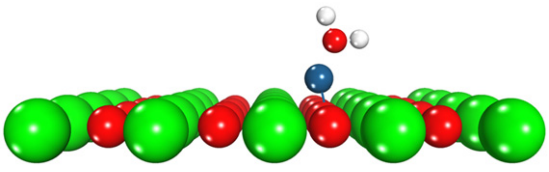

Pt mediates the charge transfer from $SrTiO_3$ to H_2O and can improve the efficiency of photocatalytic water splitting.

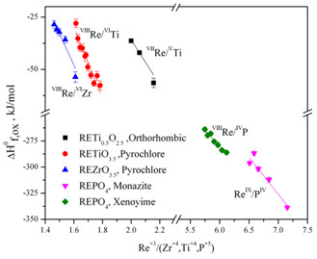

Normalized enthalpy of formation for one RE^{3+} cation from the oxides for several RE ternary oxide systems *vs.* the cation radius ratio R_A/R_B (A = RE, B = Ti, Zr, P). All the RE ternary oxide systems are stable relative to constituent oxides, with increasing stability as R_A/R_B increases. The Roman numerals above the cations represent the coordination number.

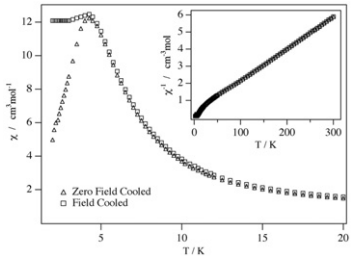

$Nd_{18}Li_8Fe_4TiO_{39}$ undergoes a transition to a spin-glass state at 4.25(5) K.

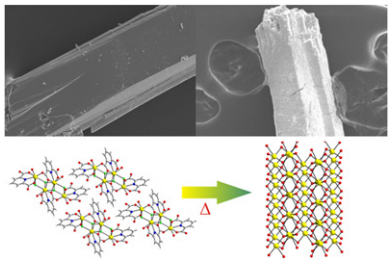

Calcination of the $Bi[NC_5H_3(CO_2)_2](OH_2)F$ single crystals at 800 °C results in the α-Bi_2O_3 rods that maintain the original morphology of the crystals.

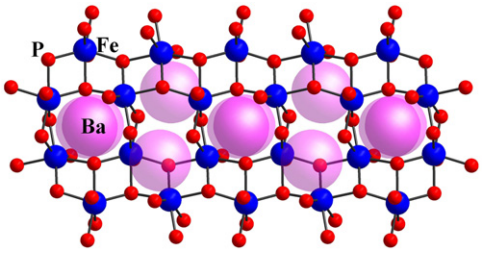

$Ba(H_2O)M_2^{III}[PO_3(OH)]_4$ (M = Fe, V) varies in space group from $P2_1$ to $P2_1/c$, arising from ordered to disordered distributions of Ba^{2+} and H_2O in the cavities.

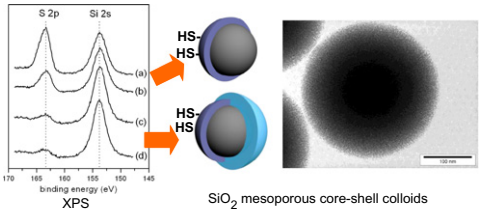

Mesoporous core shell SiO_2 colloids with organized thiol groups.

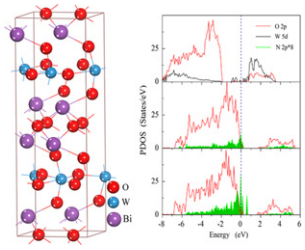

The oxygen vacancy in Bi_2WO_6 serves as a trapping center of photogenerated electrons. Nitrogen-doping improves the separation of photogenerated electron-hole pairs. Moreover, band gaps decrease obviously with doping concentration increasing.

Continued

Luminescence properties of core-shell structured SiO_2@$CaMoO_4$:Eu^{3+} phosphor

Xiaoxia Ju, Xueming Li, Yuling Yang, Wulin Li, Chuanyi Tao and Wenlin Feng

page 109

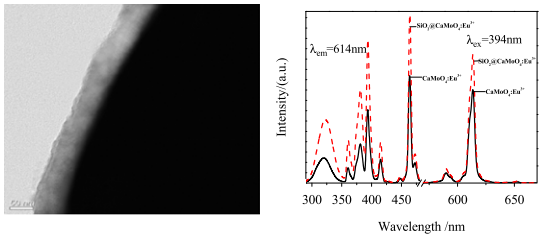

A SiO_2 nano-layer with thickness of 60 nm and good uniformity was successfully coated on the surface of $CaMoO_4$:Eu^{3+} phosphor. This coating greatly increases luminescent intensity of the phosphor.

The system Ta–V–Si: Crystal structure and phase equilibria

A.U. Khan, P. Broz, H.Y. Niu, J. Bursik, A. Grytsiv, X.-Q. Chen, G. Giester and P. Rogl

page 114

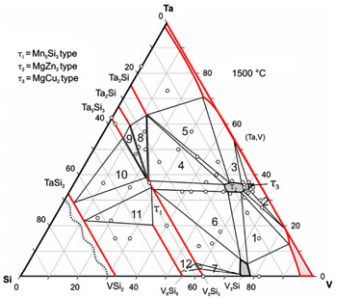

Phase relations have been evaluated for the Ta–V–Si system at 1500 and 1200 °C.

Synthesis, crystal structure, and electrode characteristics of $LiMnPO_4$(OH) cathode for lithium batteries

Yang Yang, Masaaki Hirayama, Masao Yonemura and Ryoji Kanno

page 124

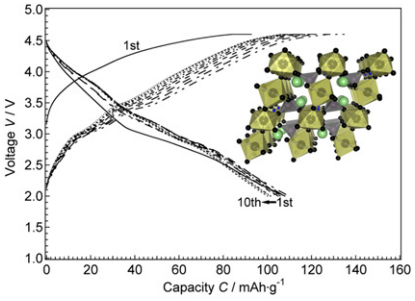

Tavorite-type material $LiMnPO_4$(OH) shows lithium intercalation at an average voltage of 3.4 V (vs. Li) after a phase transition during the first charge–discharge.

Microwave-assisted low temperature synthesis of wurtzite ZnS quantum dots

Robina Shahid, Muhammet S. Toprak and Mamoun Muhammed

page 130

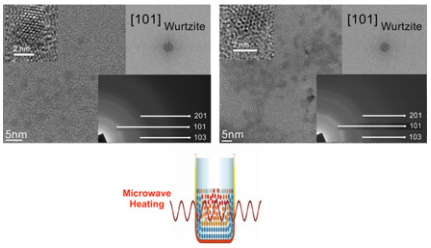

Microwave assisted synthesis of wurtzite ZnS quantum dots (QDs) have been achieved in controlled reaction at temperature as low as 150 °C. The synthesis was performed in different microwave absorbing solvents with multisource or single source precursors for very short reaction periods due to effective heating with microwaves.

Pressure response of vacancy ordered maghemite (γ-Fe_2O_3) and high pressure transformed hematite (α-Fe_2O_3)

Giovanni Hearne and Vittoria Pischedda

page 134

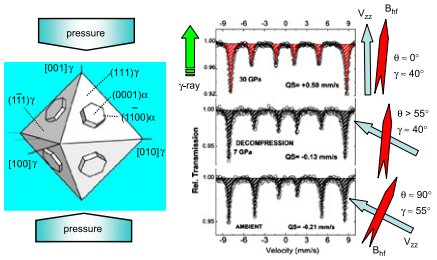

Pressure instigated topotactic transformation of vacancy ordered γ-$Fe_2O_3 \rightarrow \alpha$-$Fe_2O_3$. There is restricted spin (B_{hf}) reorientation in the new pressure transformed hematite due to entrapped vacancies. The change in direction of V_{zz} signifies a distortion of the FeO_6 octahedral local environment.

Versatile lanthanide-azide complexes with azide/carboxylate/hydroxy mixed bridged chain exhibiting magnetic and luminescent properties

Hai-Chao Wang, Min Xue, Qian Guo, Jiong-Peng Zhao, Fu-Chen Liu and Joan Ribas

page 143

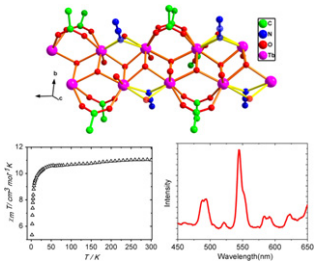

Two new 1D lanthanide-azide complexes, $[Ln_2(N_3)(isonic)_2(OH)_3(Hisonic)(H_2O)]_n$ (Ln = Yb^{III} for **1** and Tb^{III} for **2**, isonic = isonicotinate), were synthesized by hydrothermal reaction and exhibit interesting magnetism and fluorescence properties.

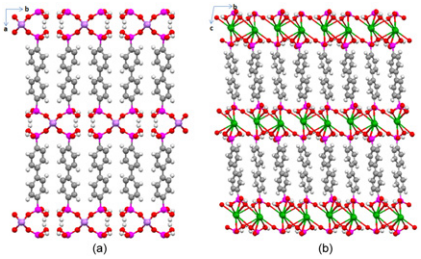

Two of five metal biphenylenebisphosphonate structures (lithium (a) and cesium (b)) are presented. Each compound is a potential Bronsted acid catalyst, where three of the original four protons are retained from the biphenylenebisphosphonic acid.

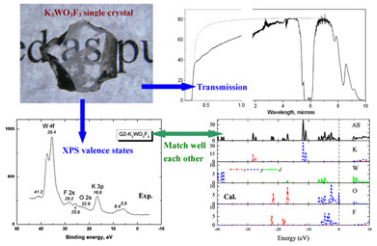

Using the cm-size $K_3WO_3F_3$ crystal (left upper), the transmission spectrum (right upper) and XPS valence electronic states (left lower) were measured, agreed with the *ab initio* results (right lower).

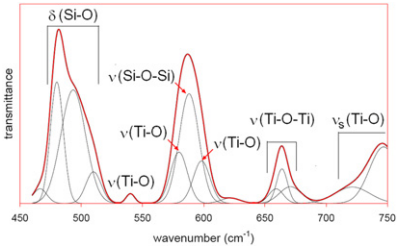

The Pechini synthesis of $(Ba, Sr)_2TiSi_2O_8$ titano-silicate fresnoites delivers finely divided precursors for applications as diverse as solid electrolytes and photocatalysis that exploit the unique Ti–O and Si–O bonding and structural morphology of these materials.

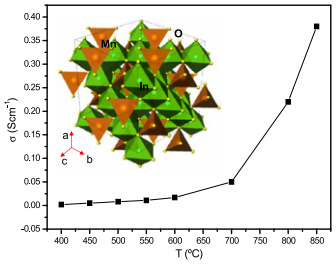

From NPD data the crystallographic formula $(Mn_{0.924(2)}In_{0.076(2)})_{8d}(In_{1.804(2)}Mn_{0.196(2)})_{16d}O_4$, shows a slight degree of inversion, $\lambda = 0.08$ and a certain In deficiency. The presence of Mn ions, able to adopt mixed oxidation states, localize the charges that, otherwise, would be delocalized in the spinel conduction band;
the presence of localized Mn^{2+} and Mn^{3+} ions provides the characteristic brown color.

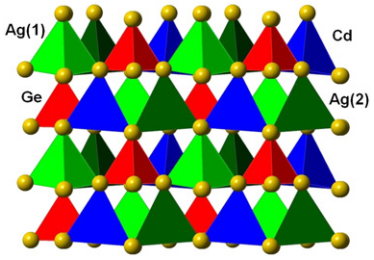

The structure of the diamond-like semiconductor Ag_2CdGeS_4 has been solved and refined in the orthorhombic noncentrosymmetric space group $Pna2_1$. A view down the *a*-axis shows that all MS_4 tetrahedra are pointing in the same direction along the *c*-axis. The structure can be derived from that of lonsdaleite.

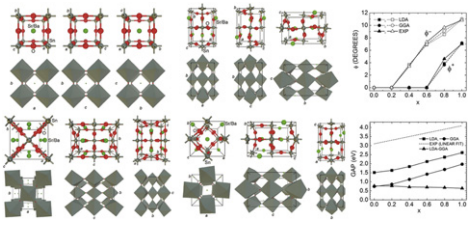

Continued

In-situ non-ambient X-ray diffraction studies of indium tungstate

Tamam I. Baiz, Christophe P. Heinrich, Nathan A. Banek, Boris L. Vivekens and Cora Lind

page 195

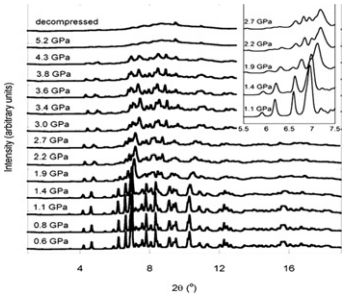

Variable pressure X-ray diffraction patterns of $In_2W_3O_{12}$ collected in a diamond anvil cell. A phase transition is clearly observed between 2.2 and 2.7 GPa, followed by irreversible amorphization.

The polygallides: $Yb_3Ga_7Ge_3$ and $YbGa_4Ge_2$

Sebastian C. Peter, Christos D. Malliakas, Heinze Nakotte, Karunakar Kothapilli, Sudhindra Rayaprol, Arthur J. Schultz and Mercouri G. Kanatzidis

page 200

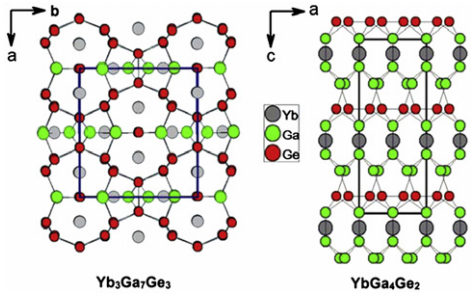

The compounds $Yb_3Ga_7Ge_3$ and $YbGa_4Ge_2$ are obtained from reactions of Yb and Ge in excess liquid gallium.

Structural analysis of Li-intercalated hexagonal boron nitride

A. Sumiyoshi, H. Hyodo and K. Kimura

page 208

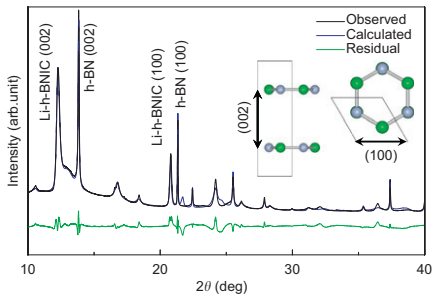

XRD pattern fitting of the sample and schematic view of host h-BN lattice.

First-principles studies of Ni–Ta intermetallic compounds

Yi Zhou, Bin Wen, Yunqing Ma, Roderick Melnik and Xingjun Liu

page 211

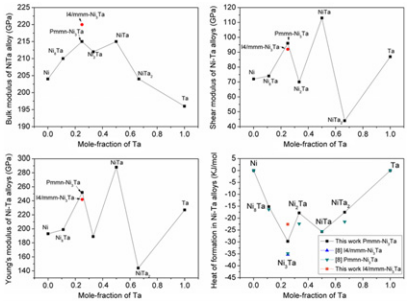

Mechanical properties and formation heats of Ni–Ta intermetallic compounds are discussed in detail in this paper.

Effect of the Keggin anions on assembly of Cu^I-bis(tetrazole) thioether complexes containing multinuclear Cu^I-cluster

Xiu-Li Wang, Qiang Gao, Ai-Xiang Tian, Hai-Liang Hu and Guo-Cheng Liu

page 219

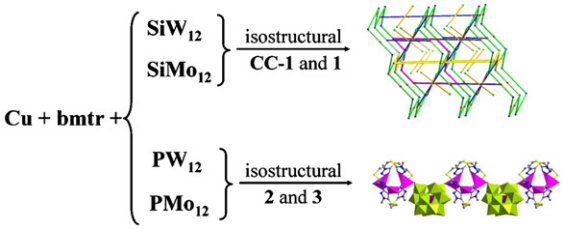

Three new complexes based on different Keggin anions and multinuclear Cu^I-cluster have been synthesized under hydrothermal conditions. The Keggin polyanions with different central heteroatoms play a key role.

Structural and magnetic characterisation of $CoSb_2O_4$, and the substitution of Pb^{2+} for Sb^{3+}

Benjamin P. de Laune and Colin Greaves

page 225

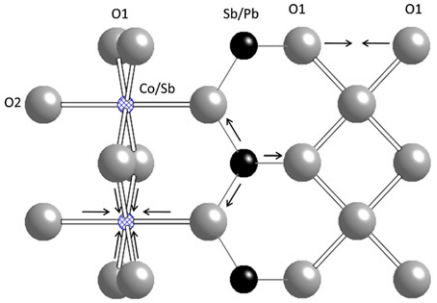

Structural changes on substitution of Pb^{2+} ions for Sb^{3+} ions in $CoSb_2O_4$.

Structure–property correlation in epitaxial (2 0 0) rutile films on sapphire substrates
M.R. Bayati, Sh. Joshi, R. Molaei, R.J. Narayan and J. Narayan
page 231

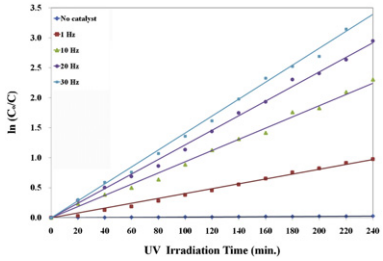

In this report, epitaxial rutile TiO_2 thin films were deposited by PLD process under various deposition rates (frequencies) and their physical and chemical properties, especially photocatalytic performance, were investigated. It was found that photocatalytic efficiency improves when frequency increases. This behavior was mainly related to formation of point defects which enhance the charge separation.

Magnetic properties and magnetocaloric effect in $La_{0.7}Nd_{0.3}Fe_{13-x}Si_x$ compounds
S. Mican and R. Tetean
page 238

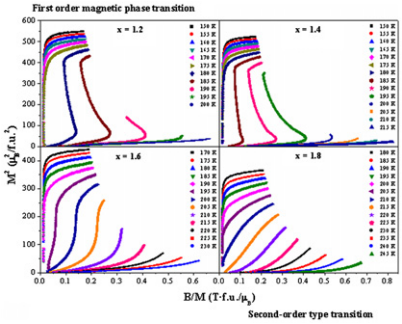

Transition from a first-order to a second-order magnetic phase transition at T_C on $La_{0.7}Nd_{0.3}Fe_{13-x}Si_x$.

The hydrogenation of Dy_5Pd_2 followed by *in situ* methods
H. Kohlmann, E. Talik and T.C. Hansen
page 244

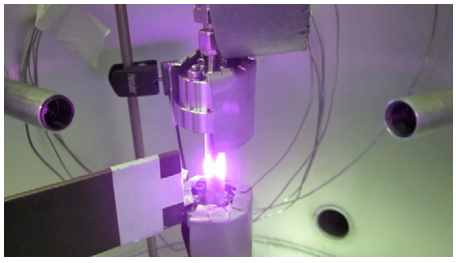

The hydrogenation of Dy5Pd2 is being followed by *in situ* neutron diffraction.

Low-temperature synthesis, luminescence and phonon properties of Er and/or Dy doped $LaAlO_3$ nanopowders
Mirosław Mączka, Esmeralda Mendoza-Mendoza, Antonio F. Fuentes, Karol Lemański and Przemysław Dereń
page 249

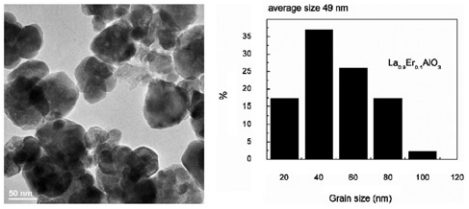

TEM image of $La_{0.9}Er_{0.1}AlO_3$ (left panel) and histogram showing the particle size distribution (right panel).

Substitutions into the trigonal bipyramidal site of $InGaCuO_4$
Rosa Grajczyk, Krishnendu Biswas, Romain Berthelot, Jun Li, A.W. Sleight and M.A. Subramanian
page 258

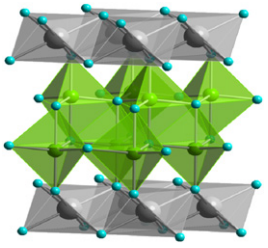

Solid solutions of $InMCu_{1-x}Mg_xO_4$ ($M = Ga^{3+}$, Al^{3+}) have been synthesized and analyzed with powder X-ray and neutron diffraction, dielectric and magnetism measurements. A shift in the lattice parameters that cannot be explained by the change in ionic radii is addressed through a study of the trigonal bipyramidal site.

Two new ternary lanthanide antimony chalcogenides: $Yb_4Sb_2S_{11.25}$ and $Tm_4Sb_2Se_{11.68}$ containing chalcogenide Q^{2-} and dichalcogenide $(Q_2)^{2-}$ anions
Jean-Marie Babo and Thomas E. Albrecht-Schmitt
page 264

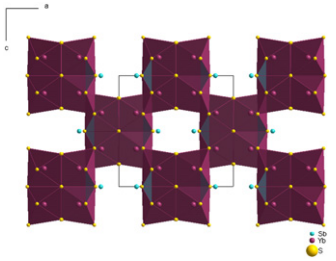

The crystal structure of $Yb_4Sb_2S_{11}$ viewed along the [0 1 0].

Continued

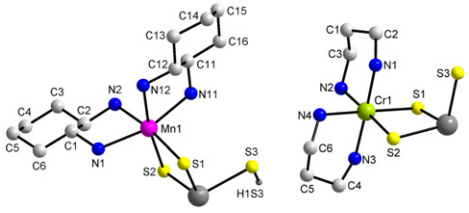

The two new compounds $[Mn(1,2\text{-chxn})_2SbS_3H]$ and $[Cr(1,3\text{-dap})_2SbS_3]$ contain the SbS_3^{3-} anion acting as bidentate ligand.

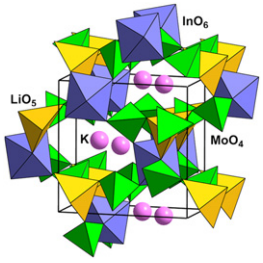

Exploring the Li_2MoO_4–K_2MoO_4–$In_2(MoO_4)_3$ system showed its partial non-quasibinarity and revealed new compounds $K_3InMo_4O_{15}$ (isotypic to $K_3FeMo_4O_{15}$) and $LiK_2In(MoO_4)_3$ which were structurally studied. An open framework of the latter is formed by vertex-shared MoO_4 tetrahedra, InO_6 octahedra and LiO_5 tetragonal pyramids.

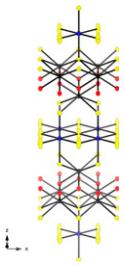

The structure of $UEr_2O_2S_3$ U/Er, black; Er, blue; O, red; S, yellow.

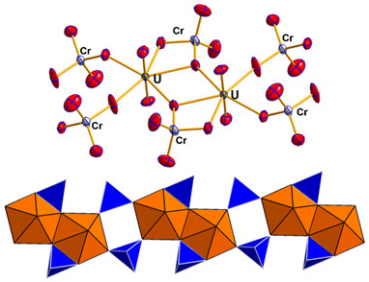

Uranyl chromate chain with monodentate and bidentate coordination mode of uranyl cations by CrO_4 tetrahedra in $Cs_2(UO_2)(CrO_4)_2$.

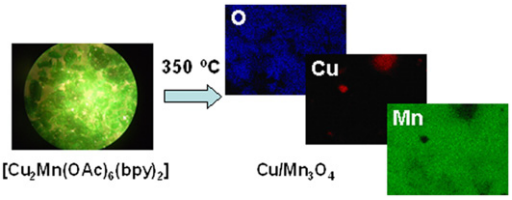

From the selective transformation of heterometallic (Zn–Mn or Cu–Mn) carboxylate complexes, it was possible to get either well defined spinel $ZnMn_2O_4$ over zinc oxide or well dispersed copper particles surrounded by a manganese oxide (Mn_3O_4) in a core-shell like structure.

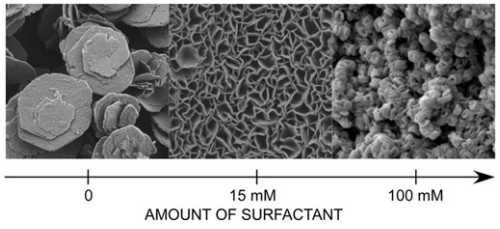

Dependence of ZnAl LDH Morphology on SDS concentration.

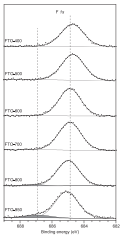

The influence of fluorination on the surface of TiO_2 by thermal shock method at several temperatures has been investigated by following the evolution of the F1*s* spectra obtained by X-ray photoelectron spectroscopy. The blank peaks are assigned to the chemisorbed fluoride ions on the samples surface and the filled peaks to fluorine atoms in oxygenated environment of solid solution $TiO_{2-x}F_x$, which is originated from the substitution of F ions for O ions in the TiO_2 lattice.

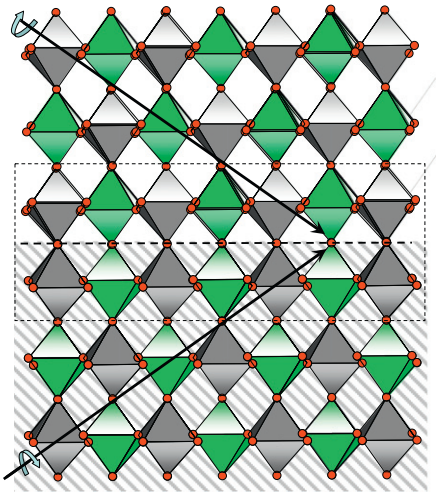

The intergrown microstructure at very fine scales within the *R3c* rhombohedral phase matrix of BNT, originating from octahedral tilt twinning disorder, will increase with respect to an external field.

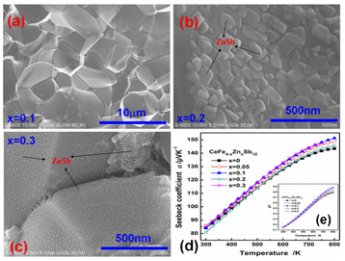

(a)–(c) ZnSb nanoinclusions emerge when Zn exceeds its solubility limit. (d), (e) The introduction of Zn boosts the Seebeck coefficient and thus enhances the *ZT* value.

Rapid Communication

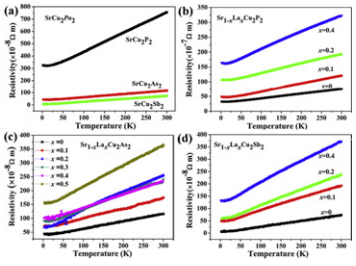

$Sr_{1-x}La_xCu_2Pn_2$ (*Pn* = P, As, Sb) show metal-like conducting behavior and no superconductive transition was observed from 300 K down to 2 K.